Article

Structural and Surface Properties of pH-Varied Fe_2O_3 Nanoparticles: Correlation with Antibacterial Properties

Farzana Naushin,[⊥] Srishti Sen,[⊥] Mukul Kumar,[⊥] Hemang Bairagi,[⊥] Siddhartha Maiti,
Jaydeep Bhattacharya,* and Somaditya Sen*

Read Online

ACCESS | Metrics & More | Article Recommendations

ABSTRACT: Hematite (Fe_2O_3) nanoparticles were synthesized using a hydrothermal synthesis route under different pH conditions (pH ∼8,10,11.5) (i.e., different ratios of H^+/OH^- ions). The sample synthesized at pH 10 had better motility toward the bacterial surface due to having an overall positive charge (ξ-potential = +11.10), leading to a minimal hydrodynamic size (D_τ = 186.6). The results are discussed in light of the relative ratio of H^+/OH^- that may affect bond formation by influencing the electronic clouds of the participating ions that can modify the structure. This, in turn, modifies crystallinity, strain, disorder, surface termination, and thereby, the surface charge, which has been correlated to the antibacterial properties of the nanoparticles due to the interaction between the respective opposite charges on the nanoparticle surface and bacterial cell wall. The structural modifications were correlated to all of these parameters in this work.
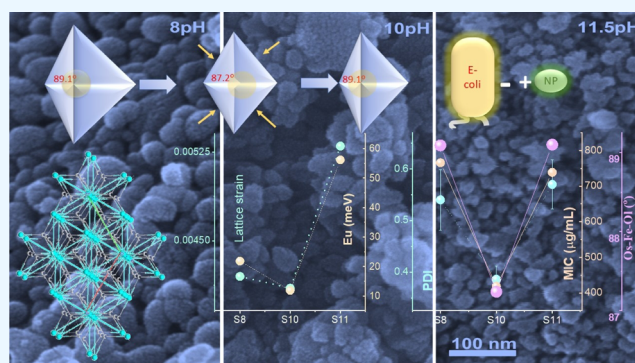
INTRODUCTION

Simple oxide nanoparticles play essential roles in various fields such as chemistry, physics, material science, and biology. Their electronic properties make them suitable for various sensors, conductors, and rectifiers.[1,2] The low toxicity and biodegradability of these nanoparticles make them widely acceptable for several biomedical applications,[3] like diagnosis, implants, wound healing, sustained drug release, and antimicrobial activity.[4−7] A leading interest is in the antibacterial properties.[4] Atomic-level chemical modifications can modify the electronic and optical properties of these materials.[8] The morphology and size of these nanoparticles can be crucial toward the applicability due to several reasons, including the surface charge properties. Such modifications can alter the effectiveness of these nanoparticles in bioapplications, especially related to the interaction of these with bacteria and other organisms.[9,10] Fe-oxides have been thoroughly studied in the field of bioapplications.[11] Depending on the different oxidation-states of Fe,[12] synthesis and characterization of α-Fe_2O_3 nanoparticles by simple coprecipitation method,[13] the literature is rich with reports on hematite (α-Fe_2O_3), maghemite (Fe_3O_4), and magnetite (γ-Fe_3O_4) having different crystal structures.[14]

Hematite, α-Fe_2O_3, is an n-type semiconductor[15] with a bandgap corresponding to visible-light energy (E_g = 2.1 eV). Hematite is known for multiple important aspects and has been the subject of intense investigation. One such critical area

is being investigated on contemporary applications of Fe_2O_3 in different forms such as co-doped Fe_2O_3, nanocomposites of α-Fe_2O_3-GO, rGO/g-C_3N_4/Fe_2O_3-heterojunctions, g-C_3N_4/α-Fe_2O_3/V_2O_5, etc. to investigate ammonia sensing, photocatalytic degradation, H_2-evolution reaction, photodegradation performance of mixed pollutants and catalytic oxidation of toluene.[16−19] Hematite is nontoxic, can be quickly produced, and has good corrosion resistance and antibacterial properties.[20] Among numerous solution/vapor-based techniques, precipitation/hydrothermal synthesis can generate nanoparticles of different shapes and morphology[21] by altering the temperature, pressure, ambient chemical conditions, precursors, and pH of the solution.[22] pH, being a precise measure of the relative concentration of H^+ (a proton) and OH^- (a hydroxyl) ions in the solution,[22] can control the electronic charge distribution of participating ions. Hence, it is an essential factor affecting the nature and details of the formation of bonds of synthesized materials, thereby modifying its structure. Different surface terminations may lead to different surface charges.[23] Antibacterial properties depend on the
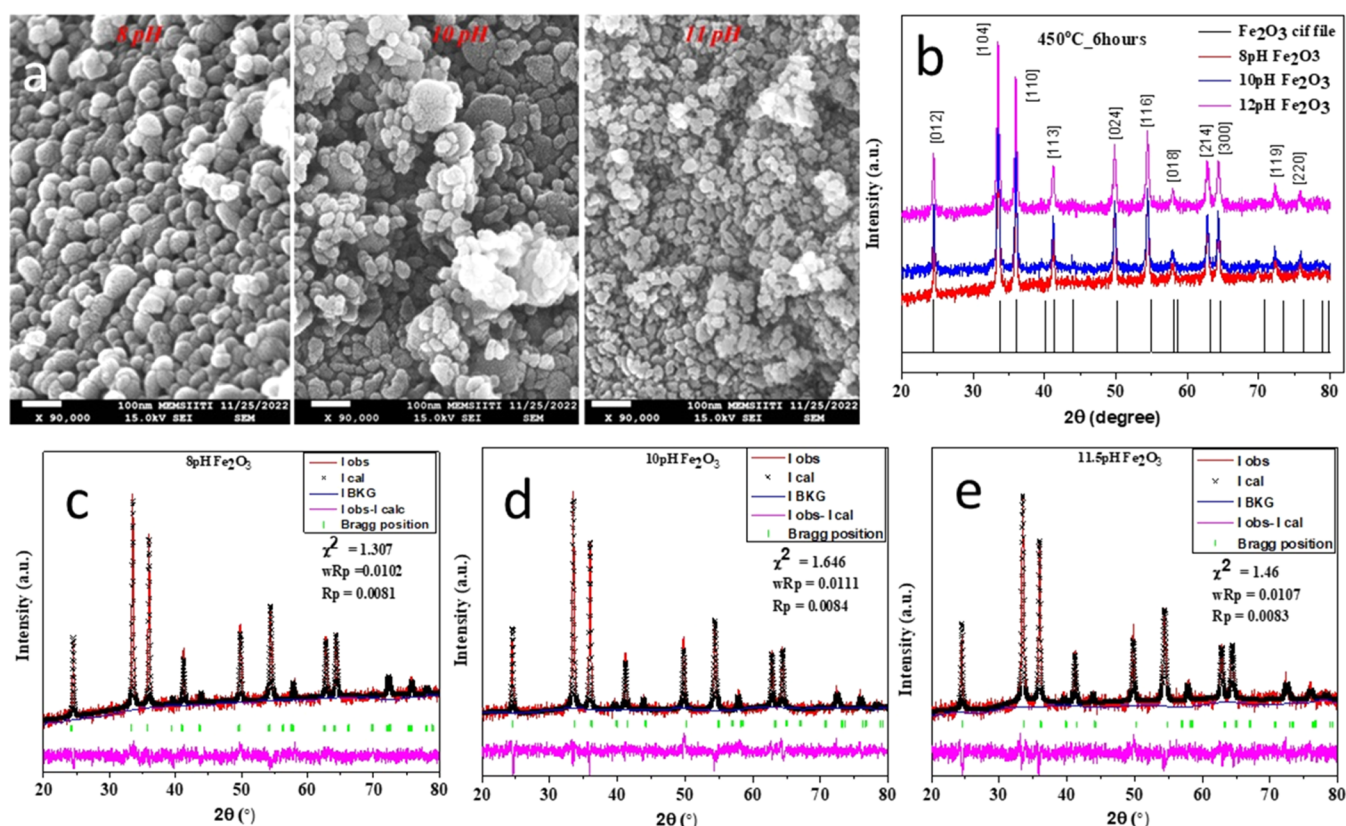
Figure 1. (a) FESEM images of the three samples revealing the reduced particle sizes of the samples from S8 to S11. These also reveal smaller nanodots of the size <5 nm adhered to the surface of the nanoparticles. (b) XRD data revealing known peaks of structure. (c−e) Rietveld refinement of XRD of the S8, S10, and S11 samples revealing excellent agreement between theory and experiment.

electrostatic forces between such surface charges and the bacterial surface charge. Hence, the formation conditions may be correlated to such antibacterial properties, an exciting field of study.[24] An attempt is being made to correlate such possibilities by taking α-Fe_2O_3 nanoparticles and *Escherichia coli* DH5α as a combination. This work emphasizes the correlation between the synthesis conditions influencing the growth parameters, which thereby changes the crystallographic parameters, leading to changes in surface charge proportions that in turn control the antibacterial properties.

■ METHODS

Synthesis of Nanoparticle. Hematite nanoparticles were synthesized via a precipitation method, using iron nitrate $(Fe(NO_3)_3 9H_2O)$ (Alfa Aesar ACS 98−101%) (salt) and ammonium hydroxide (AR-grade NH_4OH (SDFCL 25% Sp. Gr 0.91)) (base/precipitating agent). Three samples were synthesized, with the pH values of the synthesis solutions kept at 8, 10, and 11.52. These samples were named S8 for pH ~8, S10 for pH ~10, and S11 for pH ~11.52. For all samples, 12 g of iron nitrate was dissolved in 100 mL of double-distilled water and uniformly stirred on a magnetic stirrer at 250 RPM for 45 min. Ammonium hydroxide was added dropwise to obtain the desired pH values while stirring. Precipitation occurred at room temperature. Maximum yield was ensured by heating the solutions to ~60 °C. The solutions were dried at 60 °C to obtain the dried powders. These were calcinated thereafter at 450 °C in a muffle furnace for 6 h.

Characterization of Nanoparticle. *Field Emission Scanning Electron Microscopy (FESEM) and Energy-Dis-*

persive X-ray Spectroscopy (EDX) Analysis. A Supra55 Zeiss field emission scanning electron microscopy (FESEM) instrument[25] was used to obtain images at 15 kV with 15 K magnification to study the morphology and particle size. Two-dimensional (2-D) energy-dispersive X-ray spectroscopy (EDX) was performed using the same FESEM with an attached EDX analyzer.

X-ray Diffraction (XRD) Study. XRD studies[25] were performed using a Bruker D2 Phaser X-ray diffractometer. Lattice parameters, bond lengths, and bond angles were extracted from a detailed Rietveld refinement[26] of the XRD data using GSAS software. The crystallite size was calculated using the Scherrer equation[27] $D = 0.9\lambda/(\beta \times \cos(\theta))$ (where β is the fwhm of XRD peaks and D is the crystallite size),[28] while the lattice strain was calculated using Williamson−Hall equation:[29] $\beta_{total} (\cos(\theta)) = 0.9\lambda/D + 4\varepsilon \sin(\theta)$[30,31] (where ε is the lattice strain and λ is the X-ray wavelength of Cu(Kα)).

Dynamic Light Scattering [DLS] and Zeta-Potential [ζ-Potential] Measurements. The hydrodynamic size (D_τ)[32] of the nanoparticles, along with their polydispersity index (PDI) values,[33] were obtained from DLS measurements[34] using Malvern Zetasizer (Nano series). 1 mg/mL of each sample (S8, S10, S11) was prepared in filtered MilliQ and sonicated for 30 min at 25 °C to form a homogeneous solution. For the D_τ and PDI measurements, the homogeneous solution of each sample was transferred to a disposable cuvette (ZEN040), and for the ζ-potential (V_ζ)[35−38] measurements, the samples were transferred to specialized U-shaped ζ-cuvettes (DTS1070). Manual readings were taken for six cycles, with three measurements each.
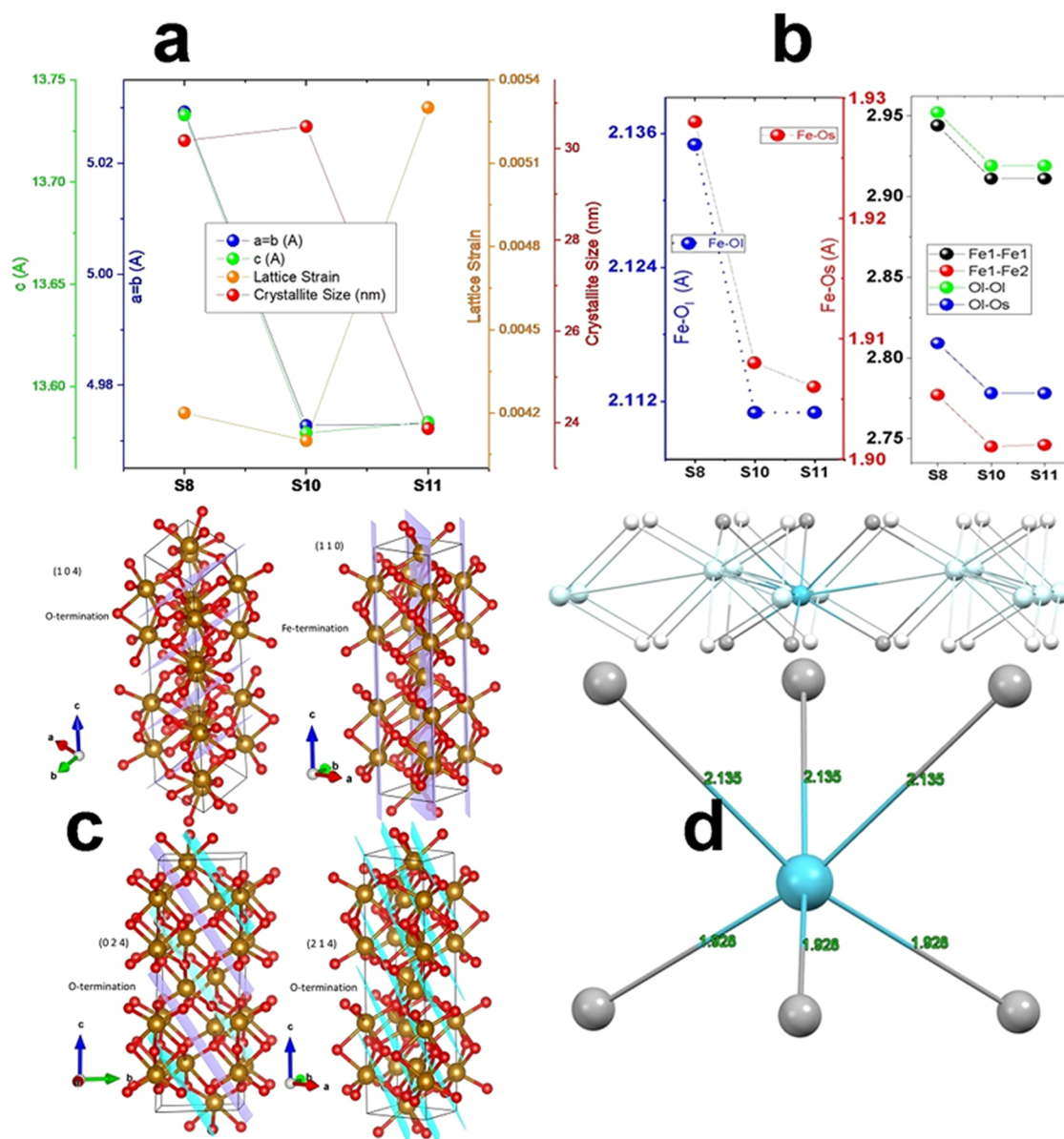
Figure 2. (a) Lattice parameter shortens considerably from S8 to S10 and nominally modifies for S11; lattice strain is minimal in S8, which enables the crystallite size to be maximum for the samples. (b) Bond lengths decrease considerably with the increase of pH from 8 to 10; after that changes nominally for the S11 sample. (c) Different planes of the Fe_2O_3 structure showing different construction indicating terminations with either O or Fe. (d) Typical FeO_6 octahedron revealing three longer $Fe-O_l$ bonds and three shorter $Fe-O_s$ bonds, indicating a noncentrosymmetric location of the Fe atom.

UV−Visible Spectroscopy Analysis. The UV−vis diffuse reflectance spectra were measured using a UV−vis (Research India Spectrophotometer) for all of the samples in the range of 200−800 nm. The direct and indirect bandgap[39] and lattice disorder (E_U, Urbach energy)[40] were studied using the optical reflectance, R, of the samples. The bandgap was determined from these spectra using the Kubelka−Munk function: $F(R) = (1-R)^2/2 \times R$,[41] where R is the diffuse reflectivity of the samples. The absorption coefficient, α, is close to the $F(R)$.[42] The diffuse reflectance increases drastically near the band edge. A linear region is observed near the edge.[43] The optical bandgap was calculated from energy-dependent optical absorbance data using the Tauc method.[44] Tauc equation for the bandgap energy determination is $(\alpha h\nu)^{1/n} = A(h\nu - E_g)$, where ν is the photon's frequency, h is Planck's constant, A is a proportionality constant, and E_g is the band gap. The nature of

the transition is between the conduction band (CB) and valence band (VB) determined by the power n; $n = 1/2, 3/2, 2,$ and 3 for direct allowed, direct forbidden, indirect allowed, and indirect forbidden transitions, respectively. The allowed direct and indirect bandgaps were calculated using this method. Lattice distortions can be responsible for the induction of defects. These can modify the bandgap and introduce states inside the gap.[45,46] Depending on the location of these defect states and the modification of the band edges, there is a possibility of some tailing states near the band edge. The energy associated with these states is defined as the Urbach energy E_U and can be calculated from these tail regions.[47] The value of α increases exponentially with energy $E = h\nu$ and is dependent on the value of E_U: $\alpha = \alpha_o \cdot \exp(h\nu/E_U)$,[48] where α_o is a constant. Taking the natural logarithm of both sides, one can achieve a linear relation between $\ln(\alpha)$ and

Table 1. Lattice Parameters, Crystalline Size, and Strain

sample	$a = b$ (Å)	c (Å)	particle size [FESEM] (nm)	crystallite size [XRD] (nm)	lattice strain
S8	5.02925 ± 0.00013	13.73285 ± 0.00065	20−40	30.17	0.0042
S10	4.97272 ± 0.00014	13.57733 ± 0.0007	20−35	30.48	0.0041
S11	4.97302 ± 0.00022	13.58262 ± 0.00094	10−30	23.87	0.0053

E: $ln[\alpha] = ln[\alpha_o] + (E/E_U)$. This allows one to estimate E_U from the linear fitting of the linear region found in ln α vs E plots.

Antibacterial Property: Minimum Inhibitory Concentration Calculation. The viability of Gram-negative bacteria, namely, *E. coli* DH5α ATCC 25922, was examined for the antibacterial application of the S8, S10, and S11 nanoparticles. All nanoparticles were initially sterilized by using ethanol. Bacterial cells were revived, and a master plate was prepared. A single colony was picked and inoculated in Luria−Bertani broth (LB). This primary culture was overnight incubated at 37 °C, at 200 rpm. From the primary culture, a secondary culture was prepared with 0.5 optical density (OD). The bacterial culture was then exposed to various concentrations of nanoparticles, and only LB medium served as a negative control. Nanoparticles alone served as a particle control. Plates were incubated at 37 °C for 18 h; OD at 600 nm was measured, and the percentage of cell viability was calculated.[49] All experiments were triplicated, and a one-way ANOVA test was applied to check the statistical differences between the control and the concentrations of particles.

RESULT AND DISCUSSION

FESEM and EDX. The FESEM images (Figure 1a) revealed agglomerated spherical nanoparticles of size 20−40 nm, with a few of them having a larger size. However, upon close inspection, all particles, irrespective of size, can be observed to be composed of further smaller nanodot-like structures of size <5 nm. Hence, the primary nanoparticles for all three samples are of size ~ 4−5 nm. The average size of the agglomerated particles for S10 seems smaller than the S8 sample. However, the S11 sample revealed much smaller particles of 10−30 nm. The dotlike surface morphology was present in the S11 sample but was less detectable due to the charging nature of the sample. This revealed a lesser conductive nature of the S11 sample.

2-D EDX scans revealed the presence of only Fe and O and the absence of any other elements, proving the phase purity of the samples.

XRD. XRD studies revealed a crystalline trigonal hematite **α-Fe_2O_3** [space group $R\bar{3}c$] structure for all of the samples (Figure 1b−e). The XRD patterns reveal reflections from the following crystallographic planes: [012] at ~24.5°, [104] at ~33.4°, [110] at ~35.94°, [113] at ~41.2°, [024] at ~49.8°, [116] at ~54.4°, [018] at ~57.9°, [214] at ~62.8°, [300] at 64.4°, [119] at ~72.3°, and [220] at ~75.8°. These peaks are commonly observed for all hematite samples, but their relative intensities seem to be modified, which generally can be correlated to the preferential exposure of certain crystallographic planes. Rietveld refinement[50] of the XRD data was performed using GSAS software to extract the structural details (Figure 2a). The lattice parameters $a = b$ were found to be maximum for S8 (~5.02925 Å) than a much smaller S10 (~4.97272 Å) and S11 (~4.97302 Å) (Figure 2a). The lattice parameter 'c' revealed a minimum for S10 (~13.57733 Å) with

a comparable but larger S11 (~13.58262 Å) and a much larger S8 (~13.73285 Å) [Table 1].

Hence, the unit cell volume of S10 is the least followed by S11, compared to a much larger S8. Therefore, the density is the highest for S10. The structure is affected by the pH of the preparation solvent. Such subtle changes bear their roots in changing the bond lengths and bond angles, which are dependent on the properties of the electronic hybridization during the bonding process.

The refined Crystallographic Index Files (CIF)[51] were analyzed using Mercury software. Bond lengths and angles were extracted. The structure of Fe_2O_3 is an arrangement of FeO_6 octahedra with an O-lattice and a Fe-lattice.

The O-lattice consists of O-planes, with each Fe atom being connected to neighboring six O-atoms, thereby creating four longer bonds $(O-O)_l$ and two shorter bonds $(O-O)_s$ (Figure 2b). The Fe atoms are in a staggered plane between two O-planes (Figure 2d).

The Fe−Fe bonds within the same plane, $(Fe-Fe)_p$, are 2.944 Å (S8) and 2.911 Å (S10 and S11). The Fe−Fe interplanar bonds, $(Fe-Fe)_i$, between subsequent Fe-layers, are shorter than $(Fe-Fe)_p$. A significant decrease of $(Fe-Fe)_i$ from 2.777 Å (S8) to 2.745 Å (S10) and 2.746 Å (S11) is observed (Figure 2b). The O_s-Fe-O_l bond angle in FeO_6 octahedra is comparable to ~89.09° for S8 and 89.1° for S11 but is much smaller for S10 ~87.24°. However, the other two angles, i.e., O_l-Fe-O_l (~82.28°) and O_s-Fe-O_s (~99.95°) [Table 2], show nominal changes and can be considered

Table 2. Bond Angles

sample	O_l-Fe-O_s	O_l-Fe-O_l	O_s-Fe-O_s
S8	89.09°	82.28°	99.94°
S10	87.24°	82.28°	99.95°
S11	89.10°	82.27°	99.94°

unaffected by pH. The O_s-Fe-O_l angle is the least for S10, saying that the FeO_6 octahedra are most distorted and the hexacoordinated Fe is most off-centered in the O_6-cage. Two sets of three Fe−O bonds are observed with three shorter Fe−O_s bonds in one plane and three longer Fe−O_l bonds in the adjacent O-plane (Figure 2d). The distortion can also be revealed from these bond lengths. The values of Fe−O_l are 2.111 Å for both S10 and S11 but are longer for S8 ~2.135 Å, while Fe−O_s keep reducing from 1.928 Å in S8 to 1.908 Å in S10 and 1.906 Å in S11 [Table 3].

These subtle changes in the bond lengths and bond angles not only distort the FeO_6 octahedra but also have

Table 3. Bond Lengths

sample	Fe−O_l (Å)	Fe−O_s (Å)	Fe_1−Fe_1 (Å)	Fe_1−Fe_2 (Å)	O_l−O_l (Å)	O_l−O_s (Å)
S8	2.135	1.928	2.944	2.777	2.952	2.809
S10	2.111	1.908	2.911	2.745	2.919	2.778
S11	2.111	1.906	2.911	2.746	2.919	2.778

consequences on the surface terminations of different crystallographic planes (Figure 2c). The XRD data was investigated for this purpose in a different light. A comparative study was performed on subtle changes in the peak intensities of the different lattice planes. The relative peak intensities were the weakest for S8 but were comparable for S10 and S11. The peak intensities were normalized with respect to the most intense (104) peak. The relative strengths of different peaks were analyzed. Several peaks were observed corresponding to O terminations [104 (024) (214) (012)] and Fe terminations (110). In some of the planes, both O and Fe were present [(113) (116) (018) (300) (1010) (220)].

These mixed anion-cation combinations are unlikely to contribute to surface charge. Hence, the intensity ratios of the Fe/O-terminated planes were critically analyzed. It was observed that the (214) continuously decreases in intensity, revealing a decrease of the negative surface charge with increasing pH. However, all other O-planes were observed not to be affected by the pH change from 8 to 10. When the pH is raised from 10 to 11.52, the intensity of all of these oxygen planes increases. These intensity changes are nominal. On the other hand, the Fe terminated plane, i.e., (110), is unaffected for a pH change from 8 to 10 but sharply decreases for pH 11.52. There needs to be detailed theoretical work following this observation to supplement this claim.

The d-spacings of the lattice planes were also found to vary. Thus, it is evident from the structural analysis described above that the pH does modify the hybridization of the participant ions. This alters the bond lengths and bond angles, modifying the structure and preferential termination of the nanoparticles. These factors, in turn, change the surface charges of the materials.

The strain in the S8 sample is 0.0042, which nominally decreases for S10 to 0.0041 and, after that increases noticeably to 0.0053 for S11 (Figure 2a). Such changes can now be correlated to the fact that the most difference in the crystallographic planes is observed for the S11 sample. Because of strain, the average crystallite size increased nominally from ~30.17 nm for S8 to 30.48 nm for S10 and, after that, reduced to a much smaller size of ~23.87 nm for S11 [Table 1]. It is noteworthy that despite the largest crystallite size of S10, the D_τ of the same is the minimum among the three samples. This will be discussed in the following DLS measurement sections. This may be the consequence of the changing nature and magnitude of the surface charge due to the different modes of surface terminations. This seem to be correlated to the modifying bond lengths of the materials.

UV−Visible Spectroscopy. Fe_2O_3 has been reported in the literature to have both a direct and indirect bandgap. The direct and indirect bandgap[39] and lattice disorder (E_U, Urbach energy)[40] were studied using the optical reflectance, R, of the samples using a UV−vis (Research India Spectrophotometer). In this study, the direct bandgap ($E_{g\text{-direct}}$) was found to continuously increase from 2.127 eV (S8) to 2.173 eV (S10) to 2.198 eV (S11). The indirect bandgap ($E_{g\text{-indirect}}$) was found to decrease from 1.917 eV (S8) to 1.873 eV (S10) and 1.807 eV (S11) [Table 4]. However, the errors were high for both E_g-direct and E_g-indirect to add any meaningful change in E_g (Figure 3a). However, the Urbach energy reduces from 21.80 meV in S8 to 11.86 meV in S10 and, after that, increases drastically to 56.14 meV in S11 (Figure 3b). Such changes are also consistent with the changes in structural studies.

Table 4. Bandgap Analysis

sample	direct E_g (eV)	indirect E_g (eV)	urbach energy (meV)
S8	2.127 ± 0.0863	1.917 ± 0.08769	21.80 ± 1.14415
S10	2.173 ± 0.0752	1.873 ± 0.12022	11.86 ± 0.9695.
S11	2.198 ± 0.1284	1.807 ± 0.07372	56.14 ± 1.08007

V_ξ, D_τ, and PDI Measurements. DLS, also known as photon correlation spectroscopy or quasi-elastic light scattering, is a technique that primarily measures three critical parameters related to the Brownian motion of macromolecules in solution that arises due to the bombardment of solvent molecules: V_ξ, D_τ, and PDI. The motion of the nanoparticles is related to D_τ, which is the size of the cluster of nanoparticles inside a specific fluid medium. The V_ξ is an estimate of the surface charge of crystals, while the PDI is a measure of the size distribution of the particles in a sample. V_ξ can be employed to understand the physical stability of nanosuspensions.[38] If − 10 mV < V_ξ < + 10 mV, then particles are approximately neutral, while for V_ξ > + 30 mV, particles are strongly cationic, whereas for V_ξ < − 30 mV then nanoparticles are strongly anionic. A significant positive or negative value of V_ξ of nanocrystals indicates good physical stability of nanosuspensions due to the electrostatic repulsion of individual particles. For a range of − 30 mV < V_ξ < + 30 mV, the repulsive forces are generally considered insufficient to attain excellent physical colloidal stability.[52] On the other hand, a small V_ξ value can result in particle aggregation and flocculation due to the Van der Waals attractive forces acting upon them. These may result in physical instability.[53] It is the potential that is generated at the slipping plane. The slipping plane is between the fluid layer, which is electrostatically attached to the nanoparticle, and the first layer, which is part of the dynamic fluid. The values of V_ξ were − 4.85 ± 0.90 mV (S8), + 11.10 ± 0.10 mV (S10), and + 22.10 ± 1.00 mV (S11) (Figure 3c). Hence, all three samples displayed physical colloidal instability, resulting in particle aggregation and flocculation. Note that the value of V_ξ continually increases from a low negative value, as in the case of S8, to a low positive value in S10 and further to a moderate positive value in S11. The V_ξ value is the average value of the surface charge of the nanoparticles, which is the result of all surface terminations. Hence, surfaces terminating with negative O-planes dominate in S8, while the relative amount of surface terminations with positive Fe-planes increases with increasing pH. This is a remarkable result that modifies the possible surface construction due to the more fundamental nature of the ambient solution.

D_τ is the effective spherical size of the particles, which provides the same friction in the fluid as the particle itself. Mathematically, one can express $D_\tau = kT/3\pi\eta D$, where T = temperature, k = Boltzmann constant, and D = diffusion coefficient. Hence, D_τ is the diffusivity of the nanocrystals within a fluid.[54−56] The D_τ of the S8 sample was the largest ~467.1 ± 43.3 d·nm as compared to a smaller S11 ~265.9 ± 15.4 d·nm and yet smaller S10 sample ~186.6 ± 2.5 d·nm (Figure 3c). On revisiting the crystallite size one can be reminded that the sizes were ~30.17 nm for S8, ~30.48 nm for S10, and ~23.87 nm for S11. The V_ξ, being ~4 mV for S8, is nearly chargeless, resulting in an ample chance of aggregation and flocculation. Hence, the D_τ value of ~467 nm can be justified. On the other hand, the S11 sample had a V_ξ of ~ +22 mV, which is large yet less than 30 mV. Hence, the aggregation/flocculation process cannot be avoided. As a
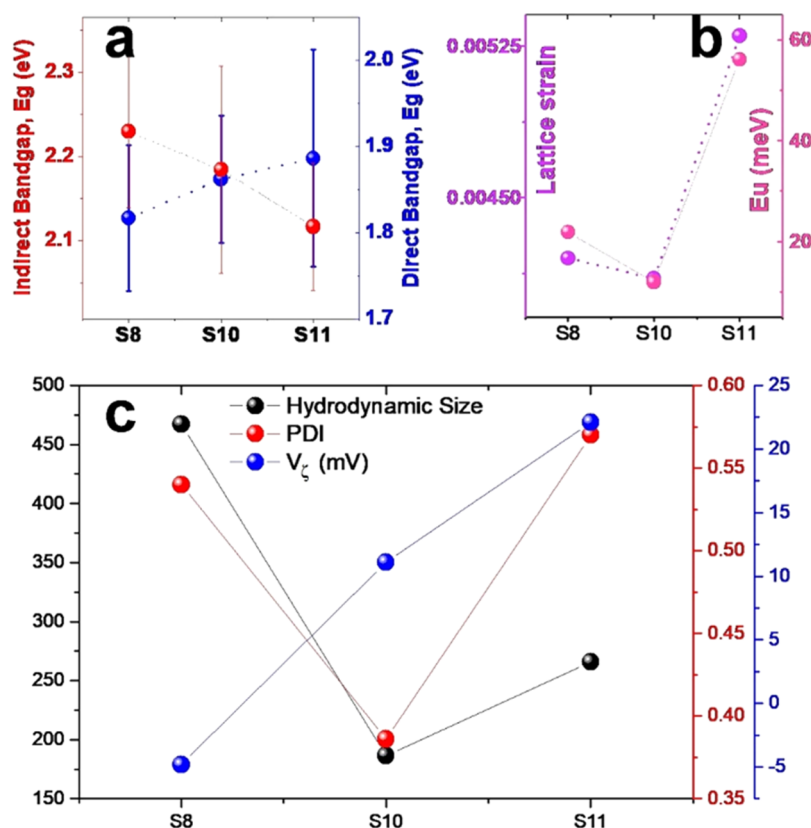
Figure 3. (a) Direct and indirect bandgaps were found to follow opposite changing patterns. (b) The Urbach energy reduces nominally from S8 to S10 but increases considerably for the S11 sample. The trend is similar to the lattice strain, indicating that the disorder is a source of strain in the lattice. (c) D_τ and PDI of the samples showed a minimum for the S10 sample, whereas the V_ζ of the S8 sample showed a negative value but that of the S10 and S11 samples revealed a positive value.

result, we see smaller D_τ values for S10 and S11. The particle sizes of these nanoparticles and their aggregation morphology must play essential roles in the final values of D_τ.

For a monodisperse sample, the PDI value must be less than 0.05, whereas extremely polydisperse materials have a PDI > 0.7. If PDI is in the range of 0.08 < PDI < 0.7, then the material is said to have midrange polydispersity, whereas samples with 0.05 < PDI < 0.08 are nearly monodisperse. PDI values of the samples were found to be 0.540 ± 0.059 (S8), 0.386 ± 0.026 (S10), and 0.570 ± 0.048 (S11) (Figure 3c) [Table 5]. All of the samples reveal midrange polydispersity. The lowest value for S10 may be correlated to the highest value of D_τ for this sample.

Table 5. D_τ, Polydispersity Index, and ζ-Potential

sample	average D_τ (d·nm)	average polydispersity index (PDI)	average V_ζ (mV)
S8	467.1 ± 43.3	0.540 ± 0.059	−4.85 ± 0.90
S10	186.6 ± 2.5	0.386 ± 0.026	11.10 ± 0.10
S11	265.9 ± 15.4	0.570 ± 0.048	22.10 ± 1.00

Antibacterial Study. The previous section discussed changes in the structural and electronic properties of the materials. An electrostatic interaction between the opposite charges of the cell walls and the nanoparticles can lead to cell wall rupture.[57] Hence, the changes in the electronic properties can be a source of modifications in the antibacterial properties of these materials. 50% of cell viability (IC_{50}) was observed at a concentration of 738.91 ± 116.7 μg/mL for S11, 418.99 ± 7.3

μg/mL for S10, and 766.05 ± 70.19 μg/mL for S8, respectively (Figure 4a). In this study, S10 revealed the lowest IC_{50} value, i.e., maximum antibacterial properties.

The negative charge of the S8 samples and the high positive charges of the S11 sample are averse to the nanoparticle-cell wall interaction. In contrast, S10, with a reasonable charge and a smaller D_τ, seems most effective as an antibacterial material.

Hence, the effect of different pH values of the ambient solution while synthesizing the Fe_2O_3 nanoparticles is noteworthy. The different ratios of H^+ and OH^- ions modify the electronic clouds of the cations and anions and, thereby, alter the bonding.

From the structure aspect, it is observed that the unit cell volume decreases, i.e., density increases, as the pH is raised from 8 to higher values. This phenomenon occurs due to the contracting bond lengths of the FeO_6 octahedra. These changes affect the lattice strain, which is a minimum for S10. As a result, the crystallite size is at a maximum for S10. This results in the crystalline disorder being the least for S10. The changes in the bond lengths are such that one of the angles O_l-Fe-O_s is drastically less for S10, which may be correlated to the monodisperse nature of the sample. These changes lead to modifications of the off-centering of the Fe atom in the FeO_6 octahedra. The surface charge of the nanoparticles were observed to change from negative to positive while pH changed from 8 to 10 and kept increasing with increasing pH. Changes in bond lengths and bond angles bring subtle changes to the surface charge and are close to a neutral value in between a pH of 8−10, where the angle is slightest. The
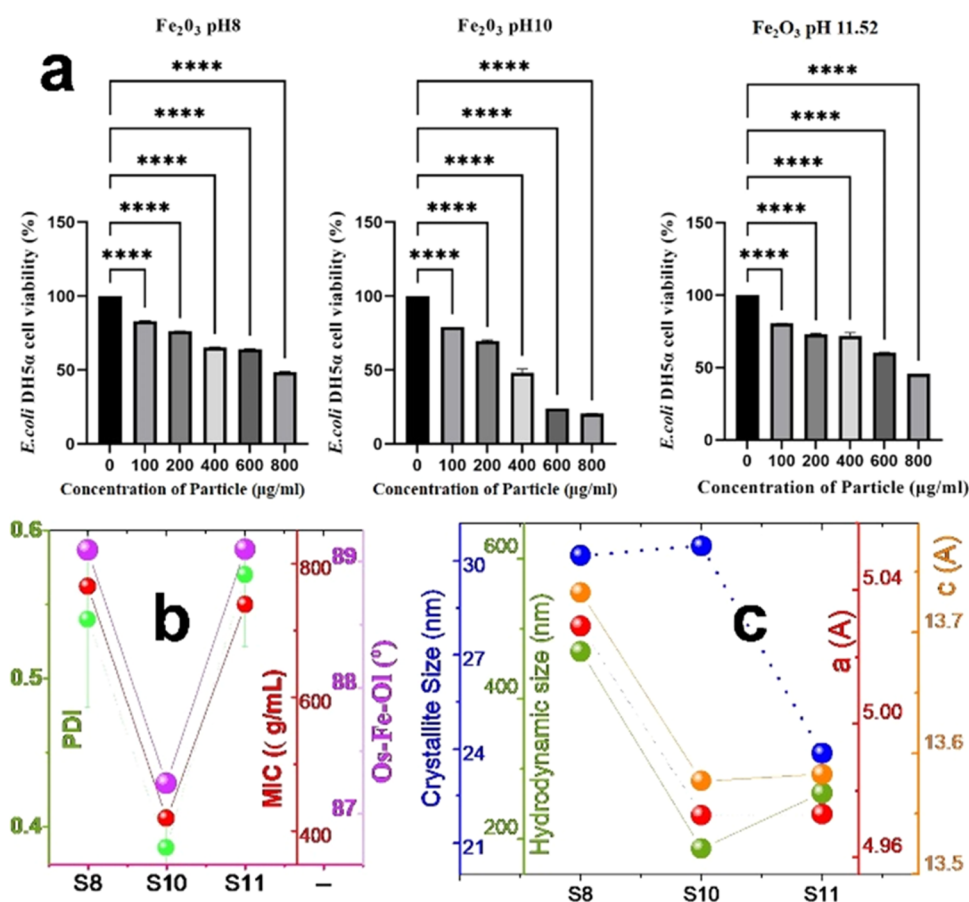
Figure 4. *(a) E. coli* cell viability at different concentrations of Fe_2O_3 nanoparticles synthesized at pH 8, 10, and 11.52. The data sets are represented as mean $\pm$ standard error of the mean ($n = 3$); one-way ANOVA test, ****$P < 0.000$. (b) Correlation between the O_s–Fe–O_l bond angle and the PDI and MIC of the samples indicating a possible mechanism of how modifications in the structure may lead to changes in the physical properties thereby affecting the biological process. (c) A similar probable correlation between lattice parameters, crystallite size, and hydrodynamic size.

negligible positive surface charge may be correlated to the monodisperse nature and nominal D_τ despite the maximum crystallite size of S10. Such a property allows more particles to be associated with the negatively charged *E. coli* bacterial cell surface, forming electrostatic interactions. The negative charge of S8 should repel the bacterial surface. Despite a higher charge, the polydisperse nature of S11 has a lesser chance of interaction.

A combination of charge properties along with the smaller D_τ (increases the population of nanoparticles on the bacterial surface, promoting greater mobility) and smaller PDI (ensures shorter separation, enabling bacterial interaction) makes S10 a better antibacterial agent than S8 and S11.

Thus, subtle changes in the chemical environment during synthesis alter bond lengths, thereby modifying factors such as surface charge and the dispersive nature of the particles, further altering antibacterial properties. This new observation needs attention from theoretical aspects and is particularly important from the biophysics interfaces of physics/chemistry.

Importance of ROS. Reactive Oxygen Species (ROS) mediated bactericidal effect is a well-known phenomenon for iron oxide nanoparticles. The Fe_2O_3 samples had a moderate bandgap of ~2.13 eV. This energy corresponds to a greenish-yellow light. An illumination of UV or white light consisting of more energetic components of light such as green, blue, violet, can hence promote an electron in the valence band (VB) to the conduction band (CB), overcoming the bandgap of the

Fe_2O_3 material, thereby leaving a hole in the VB. It is a light-assisted mechanism of the formation of an electron–hole pair in the material. The hole generated in the VB has a robust oxidizing nature. Thus, there is a light-assisted creation of oxidizing sites. These can oxidize H_2O or OH^- to produce robust oxidizing species. A redox chain reaction follows. ROS are formed, e.g., hydroxyl radical ($^\bullet OH$), hydroperoxide radical ($^\bullet H_2O_2^-$), and superoxide radical anion ($O_2^{\bullet -}$). These are the pathways of the bactericidal action. Thus, ROS generation from Fe_2O_3 samples can induce oxidative stress in the bacterial cell. Thus, e–h pair generation is an important aspect. Hence, the electronic properties of these nanoparticles should play a significant role in ROS generation and thereby affect their antibacterial activities. Mostly, the higher the ROS, the more the antibacterial property.

However, the trends of changes in the bandgap, either direct or indirect, follow a particular trend of either decreasing or increasing. On the other hand, S10 showed the lowest IC_{50} value, i.e., maximum antibacterial properties. From the V_ζ studies, one can observe positive values of the surface charge for the S10 and S11 samples. The opposite charges between the negatively charged cell membranes and the positive charges of the surface of the S10 and S11 samples result in attractive electrostatic forces. The electrostatic gradient between these two units damages the cell membranes. Hence, one can justify the response of the S10 and S11 samples toward the annihilation of the *E. coli* DH5α. A destabilization mechanism

of the charges present in the bacterial cytoplasmic membrane may happen due to electronic excitation and rupture of the membrane.

H^+ ions move across the cell membrane and generate an electrochemical gradient. It is generally observed that smaller nanoparticles can move freely over the membrane surface, and thus, the electrostatic interactions are better. Thus, the smaller D_τ of the S10 sample may be a possible reason for the better movement of these particles, and the moderately positive surface charge of ∼11.1 mV is most likely the reason for a higher probability of membrane rupture.

Thus, the enhanced antibacterial property of S10 is correlated to the positive surface charge and smaller hydrodynamic size of the particles, which is a consequence of the influence of alkalinity on the structural properties (Figure 4b,c). Further, the lowest E_U hints at a less disordered lattice, which enables the annihilation of the disorder-related tail states of the band edges, thereby raising the indirect bandgap. This less disordered lattice enables easier phonon-assisted e-h pair generation upon illumination of white light, leading to higher Reactive Oxygen Species formation.

Hence, the probable explanation of differences in ROS behind changes in antibacterial properties may not be necessary to support that S10 is the most antibacterial.[58]

CONCLUSIONS

The atmosphere of hydrothermal synthesis of hematite nanoparticles were varied with pH ∼8, 10, and 11.5. The pH affects the bonding nature of the Fe−O bonds in the FeO_6 building blocks of the α-Fe_2O_3 structure. Most of the Fe−O bonds shorten as the pH is increased from 8 to 10 and thereafter alter nominally to 11.5. Due to such bond contraction, the unit cell also contracts and thereby increases the density. The lattice strain is the least for S10, thereby modifying the crystallite size, which is the largest for S10. From the O−Fe−O bond angles, an Fe-off-centering is considered minimum for the S10 sample. This bond angle seems to influence the surface terminations and thereby modifies the surface charge from a negative value in S8 to a positive value in S10, thereby becoming higher for S11. The nominal positive charge of S10 samples is most likely the reason for the smaller D_τ and hence provides better movability of the nanoparticles in the media and, hence, approach the bacterial surface, enhancing the chance of bonding between negatively charged bacterial surfaces and positively charged S10 nanoparticles. Thus, the chances of bacterial cell rupture increases.

AUTHOR INFORMATION

Corresponding Authors

Jaydeep Bhattacharya − School of Biotechnology, Jawaharlal Nehru University, New Delhi 110067, India; Email: jaydeep@jnu.ac.in

Somaditya Sen − Department of Physics, SMART Lab, Indian Institute of Technology, Indore 453552, India; orcid.org/ 0000-0002-6129-8344; Email: sens@iiti.ac.in

Authors

Farzana Naushin − School of Biotechnology, Jawaharlal Nehru University, New Delhi 110067, India

Srishti Sen − School of Biosciences Engineering & Technology, VIT Bhopal University, Sehore, Madhya Pradesh 466114, India

Mukul Kumar − Department of MEMS, Indian Institute of Technology, Indore 453552, India

Hemang Bairagi − School of Biosciences Engineering & Technology, VIT Bhopal University, Sehore, Madhya Pradesh 466114, India

Siddhartha Maiti − School of Biosciences Engineering & Technology, VIT Bhopal University, Sehore, Madhya Pradesh 466114, India

Complete contact information is available at:
https://pubs.acs.org/10.1021/acsomega.3c05930

Author Contributions

[⊥]F.N., Srishti Sen (S.S.), M.K. and H.B. contributed equally to this work. F.N.: antibacterial studies (MIC), DLS measurements, manuscript writing. S.S.: sample preparation, XRD and UV−vis data collection, analysis of UV−vis spectroscopy, structural parameter analysis using Mercury and Vesta, correlation analysis, manuscript writing. M.K.: sample sintering, FESEM/EDX data collection, rietveld refinement of XRD data. H.B.: structural parameter analysis using Mercury and Vesta, correlation analysis, manuscript writing. S.M.: overall guidance. J.B.: mentor of biological studies. Somaditya Sen: mentor of materials studies and correlation to biological implications.

ABBREVIATIONS

w.r.t.- with respect to
D_τ- hydrodynamic size
PDI- polydispersity index
DLS- dynamic light scattering
V_ζ- ζ-potential

REFERENCES

(1) Yoon, Y.; Truong, P. L.; Lee, D.; Ko, S. H. Metal-Oxide Nanomaterials Synthesis and Applications in Flexible and Wearable Sensors. ACS Nanosci. Au 2022, 2, 64−92.

(2) Chavali, M. S.; Nikolova, M. P. Metal oxide nanoparticles and their applications in nanotechnology. SN Appl. Sci. 2019, 1, No. 607.

(3) Schneider, M. G. M.; Martín, M. J.; Otarola, J.; et al. Biomedical Applications of Iron Oxide Nanoparticles: Current Insights Progress and Perspectives. Pharmaceutics 2022, 14, No. 204.

(4) Murthy, S.; Effiong, P.; Fei, C. C. Metal oxide nanoparticles in biomedical applications. In Metal Oxide Powder Technologies; Elsevier, 2020; pp 233−251.

(5) Nikolova, M. P.; Chavali, M. S. Metal Oxide Nanoparticles as Biomedical Materials. Biomimetics 2020, 5, No. 27.

(6) Pan, S.; Goudoulas, T. B.; Jeevanandam, J.; et al. Therapeutic Applications of Metal and Metal-Oxide Nanoparticles: Dermato-Cosmetic Perspectives. *Front. Bioeng. Biotechnol.* **2021**, *9*, No. 724499.

(7) Gudkov, S. V.; Burmistrov, D. E.; Serov, D. A.; et al. Do Iron Oxide Nanoparticles Have Significant Antibacterial Properties? *Antibiotics* **2021**, *10*, No. 884.

(8) Kelly, K. L.; Coronado, E.; Zhao, L. L.; Schatz, G. C. The Optical Properties of Metal Nanoparticles: The Influence of Size, Shape, and Dielectric Environment. *J. Phys. Chem. B* **2003**, *107*, 668−677.

(9) Wysocka, A.; Łężniak, Ł.; Jagielska, E.; Sabała, I. Electrostatic Interaction with the Bacterial Cell Envelope Tunes the Lytic Activity of Two Novel Peptidoglycan Hydrolases. *Microbiol. Spectrum* **2022**, *10*, No. e00455-22.

(10) Mendes, C. R.; Dilarri, G.; Forsan, C. F.; et al. Antibacterial action and target mechanisms of zinc oxide nanoparticles against bacterial pathogens. *Sci. Rep.* **2022**, *12*, No. 2658.

(11) Cotin, G.; Piant, S.; Mertz, D.et al. Iron Oxide Nanoparticles for Biomedical Applications: Synthesis, Functionalization, and Application. In *Iron Oxide Nanoparticles for Biomedical Applications*; Elsevier, 2018; pp 43−88.

(12) Sankadiya, S.; Oswal, N.; Jain, P.; Gupta, N. *Synthesis and Characterization of Fe_2O_3 Nanoparticles by Simple Precipitation Method*, AIP Conference Proceedings; AIP: 2016.

(13) Ali, A.; Zafar, H.; Zia, M.; et al. Synthesis, characterization, applications, and challenges of iron oxide nanoparticles. *Nanotechnol. Sci. Appl.* **2016**, *9*, 49−67.

(14) Legodi, M.; Dewaal, D. The preparation of magnetite, goethite, hematite and maghemite of pigment quality from mill scale iron waste. *Dyes Pigm.* **2007**, *74*, 161−168.

(15) Zhu, M.; Wang, Y.; Meng, D.; et al. Hydrothermal Synthesis of Hematite Nanoparticles and Their Electrochemical Properties. *J. Phys. Chem. C* **2012**, *116*, 16276−16285.

(16) Ghule, B. G.; Shinde, N. M.; Raut, S. D.; et al. Self-assembled α-Fe2O3-GO nanocomposites: Studies on physical, magnetic and ammonia sensing properties. *Mater. Chem. Phys.* **2022**, *278*, No. 125617.

(17) Dang, V. D.; Khedulkar, A. P.; Adorna, J.; et al. Kinetics of the catalytic oxidation of toluene over Mn,Cu co-doped Fe2O3: Ex situ XANES and EXAFS studies to investigate mechanism. *J. King Saud Univ., Sci.* **2023**, *35*, No. 102812.

(18) Palanivel, B.; Hossain, M. S.; Raghu, M. S.; et al. Green synthesis of Fe2O3 deposited g-C3N4: Addition of rGO promoted Z-scheme ternary heterojunction for efficient photocatalytic degradation and H2 evolution reaction. *Mater. Res. Bull.* **2023**, *162*, No. 112177.

(19) Vignesh, S.; Suganthi, S.; Srinivasan, M.; et al. Investigation of heterojunction between α-Fe2O3/V2O5 and g-C3N4 ternary nano-composites for upgraded photo-degradation performance of mixed pollutants: Efficient dual Z-scheme mechanism. *J. Alloys Compd.* **2022**, *902*, No. 163705.

(20) Sirelkhatim, A.; Mahmud, S.; Seeni, A.; et al. Review on Zinc Oxide Nanoparticles: Antibacterial Activity and Toxicity Mechanism. *Nano-micro Lett.* **2015**, *7*, 219−242.

(21) Szterner, P.; Biernat, M. The Synthesis of Hydroxyapatite by Hydrothermal Process with Calcium Lactate Pentahydrate: The Effect of Reagent Concentrations, pH, Temperature, and Pressure. *Bioinorg. Chem. Appl.* **2022**, *2022*, No. 3481677.

(22) Buxton, G. V.; Greenstock, C. L.; Helman, W. P.; Ross, A. B. Critical Review of rate constants for reactions of hydrated electrons, hydrogen atoms and hydroxyl radicals (·OH/·O− in Aqueous Solution. *J. Phys. Chem. Ref. Data* **1988**, *17*, 513−886.

(23) Liu, N.; Chen, X.; Zhang, J.; Schwank, J. W. A review on TiO2-based nanotubes synthesized via hydrothermal method: Formation mechanism, structure modification, and photocatalytic applications. *Catal. Today* **2014**, *225*, 34−51.

(24) Brodusch, N.; Demers, H.; Gauvin, R. *Field Emission Scanning Electron Microscopy*; Springer Singapore: Singapore, 2018.

(25) Ryland, A. L. X-ray diffraction. *J. Chem. Educ.* **1958**, *35*, No. 80.

(26) Sakata, M.; Cooper, M. J. An analysis of the Rietveld refinement method. *J. Appl. Crystallogr.* **1979**, *12*, 554−563.

(27) Fathi, M. H.; Hanifi, A. Evaluation and characterization of nanostructure hydroxyapatite powder prepared by simple sol−gel method. *Mater. Lett.* **2007**, *61*, 3978−3983.

(28) Bushroa, A. R.; Rahbari, R. G.; Masjuki, H. H.; Muhamad, M. R. Approximation of crystallite size and microstrain via XRD line broadening analysis in TiSiN thin films. *Vacuum* **2012**, *86*, 1107−1112.

(29) Zak, A. K.; Majid, W. H. A.; Abrishami, M. E.; Yousefi, R. X-ray analysis of ZnO nanoparticles by Williamson−Hall and size−strain plot methods. *Solid State Sci.* **2011**, *13*, 251−256.

(30) Mote, V.; Purushotham, Y.; Dole, B. Williamson-Hall analysis in estimation of lattice strain in nanometer-sized ZnO particles. *J. Theor. Appl. Phys.* **2012**, *6*, No. 6.

(31) Kibasomba, P. M.; Dhlamini, S.; Maaza, M.; et al. Strain and grain size of TiO2 nanoparticles from TEM, Raman spectroscopy and XRD: The revisiting of the Williamson-Hall plot method. *Results Phys.* **2018**, *9*, 628−635.

(32) Hackley, V. A.; Clogston, J. D.Measuring the Hydrodynamic Size of Nanoparticles in Aqueous Media Using Batch-Mode Dynamic Light Scattering. In *Methods in Molecular Biology*; Springer, 2011; Vol. 697, pp 35−52.

(33) Ragheb, R.; Nobbmann, U. Multiple scattering effects on intercept, size, polydispersity index, and intensity for parallel (VV) and perpendicular (VH) polarization detection in photon correlation spectroscopy. *Sci. Rep.* **2020**, *10*, No. 21768.

(34) Bhattacharjee, S. DLS and zeta potential − What they are and what they are not? *J. Controlled Release* **2016**, *235*, 337−351.

(35) Clogston, J. D.; Patri, A. K.Zeta Potential Measurement. In *Methods in Molecular Biology*; Springer, 2011; Vol. 697, pp 63−70.

(36) Liao, D. L.; Wu, G. S.; Liao, B. Q. Zeta potential of shape-controlled TiO2 nanoparticles with surfactants. *Colloids Surf., A* **2009**, *348*, 270−275.

(37) Doane, T. L.; Chuang, C.-H.; Hill, R. J.; Burda, C. Nanoparticle ζ -Potentials. *Acc. Chem. Res.* **2012**, *45*, 317−326.

(38) Tantra, R.; Schulze, P.; Quincey, P. Effect of nanoparticle concentration on zeta-potential measurement results and reproduci-bility. *Particuology* **2010**, *8*, 279−285.

(39) Yuan, L.-D.; Deng, H.-X.; Li, S.-S.; et al. Unified theory of direct or indirect band-gap nature of conventional semiconductors. *Phys. Rev. B* **2018**, *98*, No. 245203.

(40) Ugur, E.; Ledinský, M.; Allen, T. G.; et al. Life on the Urbach Edge. *J. Phys. Chem. Lett.* **2022**, *13*, 7702−7711.

(41) Yang, L.; Kruse, B. Revised Kubelka−Munk theory I Theory and application. *J. Opt. Soc. Am. A* **2004**, *21*, No. 1933.

(42) Makuła, P.; Pacia, M.; Macyk, W. How To Correctly Determine the Bandgap Energy of Modified Semiconductor Photocatalysts Based on UV−Vis Spectra. *J. Phys. Chem. Lett.* **2018**, *9*, 6814−6817.

(43) Nowak, M.; Kauch, B.; Szperlich, P. Determination of energy bandgap of nanocrystalline SbSI using diffuse reflectance spectrosco-py. *Rev. Sci. Instrum.* **2009**, *80*, No. 046107.

(44) Estrada, R.; Djohan, N.; Pasole, D.; et al. The optical bandgap of $LiTaO_3$ and $Nb_2 O_5$ -doped $LiTaO_3$ thin films based on Tauc Plot method to be applied on satellite. *IOP Conf. Ser. Earth Environ. Sci.* **2017**, *54*, No. 012092.

(45) Khatun, N.; Rini, E. G.; Shirage, P.; et al. Effect of lattice distortion on bandgap decrement due to vanadium substitution in TiO2 nanoparticles. *Mater. Sci. Semicond. Process.* **2016**, *50*, 7−13.

(46) Dakshinamurthy, A. C.; Sudakar, C. Bandgap engineering and sublattice distortion driven bandgap bowing in Cs2Ag1- x Na x BiCl6 double perovskites. *Appl. Phys. Lett.* **2021**, *118*, No. 131902.

(47) Samiee, M.; Joshi, P.; Aidarkhanov, D.; Dalal, V. Measurement of defect densities and Urbach energies of tail states in PTB7 solar cells. *Appl. Phys. Lett.* **2014**, *105*, No. 133511.

(48) Belahssen, O.; Temam, H. B.; Lakel, S.; et al. Effect of optical gap energy on the Urbach energy in the undoped ZnO thin films. *Optik* **2015**, *126*, 1487−1490.

(49) Sarkar, S.; Thapa, R.; Naushin, F.; et al. Antibiotic-Loaded Smart Platelet: A Highly Effective Invisible Mode of Killing Both Antibiotic-Sensitive and -Resistant Bacteria. *ACS Omega* **2022**, *7*, 24102−24110.

(50) Thompson, P.; Cox, D. E.; Hastings, J. B. Rietveld refinement of Debye−Scherrer synchrotron X-ray data from $Al_2 O_3$. *J. Appl. Crystallogr.* **1987**, *20*, 79−83.

(51) Hall, S. R.; Allen, F. H.; Brown, I. D. The crystallographic information file (CIF): a new standard archive file for crystallography. *AActa Crystallogr., Sect. A: Found. Crystallogr.* **1991**, *47*, 655−685.

(52) Maguire, C. M.; Rösslein, M.; Wick, P.; Prina-Mello, A. Characterisation of particles in solution − a perspective on light scattering and comparative technologies. *Sci. Technol. Adv. Mater.* **2018**, *19*, 732−745.

(53) Margenau, H. Van der waals forces. *Rev. Mod. Phys.* **1939**, *11*, No. 1.

(54) Hackley, V. A.; Clogston, J. D.Measuring the Hydrodynamic Size of Nanoparticles in Aqueous Media Using Batch-Mode Dynamic Light Scattering. In *Methods in Molecular Biology*; Springer, 2011; Vol. *697*, pp 35−52.

(55) Gittings, M. R.; Saville, D. A. The determination of hydrodynamic size and zeta potential from electrophoretic mobility and light scattering measurements. *Colloids Surf., A* **1998**, *141*, 111−117.

(56) Pohlmeier, A.; Haber-Pohlmeier, S. Ionization of short polymethacrylic acid: titration, DLS, and model calculations. *J. Colloid Interface Sci.* **2004**, *273*, 369−380.

(57) Kumar, R.; Umar, A.; Kumar, G.; Nalwa, H. S. Antimicrobial properties of ZnO nanomaterials: A review. *Ceram. Int.* **2017**, *43*, 3940−3961.

(58) Canaparo, R.; Foglietta, F.; Limongi, T.; Serpe, L. Biomedical Applications of Reactive Oxygen Species Generation by Metal Nanoparticles. *Materials* **2021**, *14*, No. 53.